Supporting Information

Hybrid sequential processing of mixed Sn-Pb Narrow-Bandgap Perovskite Solar Cells

Yasemin Saygili, [a*] *Federico Ventosinos,* [b] *Mohammad Dehnavi,* [c] *Selçuk Yerci,* [c,d] *Michele Sessolo,* [b*] *Henk Bolink* [b]

AUTHOR ADRESS:

[a] Department of Energy Systems Engineering, Ankara University, Gölbaşı, Ankara/06830, Turkiye

[b] Instituto de Ciencia Molecular, Universidad de Valencia, C/Catedrático J. Beltrán 2, 46980 Paterna Valencia, Spain

[c] ODTU GUNAM, Middle East Technical University, Çankaya/Ankara 06800, Türkiye

[d] Department of Electrical Electronics Engineering, Middle East Technical University, Cankaya, Ankara 06800, Türkiye

* Corresponding authors

Y.S: ysaygili@ankara.edu.tr

M.S: michele.sessolo@uv.es

Experimental

Materials. All chemicals were purchased from Sigma-Aldrich, TCI, Merck KGaA, Luminescence Technology Corp, Greatcell Solar and used without further purification.

Evaporation of inorganic seed layers. Pre-patterned ITO substrates were cleaned with detergent, DI water and isopropanol, respectively, in an ultrasonic bath. A 20 min UV/O_3 treatment was performed on the cleaned substrates. The substrates were either used as HTM-free or coated with PEDOT:PSS or PTAA prior to seed layer deposition. For the samples with PEDOT:PSS, following the UV/O_3 treatment, the substates were spin coated with PEDOT:PSS with 4000rpm, for 30s. Then the films were annealed at 150°C for 10 mins. For the samples employing PTAA, 1.5mg/ml PTAA was dissolved in toluene and applied on the substates with 3000rpm, for 30s. Then the films were annealed at 100°C for 10 mins. The prepared substrates were transferred to a vacuum chamber confined within a nitrogen-filled glovebox for inorganic layer deposition. The sublimation is initiated once the pressure of the evaporation chamber is $2x10^{-6}$ mbar. PbI_2, SnI_2 and SnF_2 were co-evaporated simultaneously and the rates were set according to the desired composition. For $Pb_{0.5}Sn_{0.5}I_2$ the rates were kept as 0.5 Å s^{-1}, 0.5 Å s^{-1} and 0.03 Å s^{-1} for PbI_2, SnI_2 and SnF_2, respectively. The evaporation rates were monitored through individual QCM sensors for each of the three sources. The typical evaporation temperatures for PbI_2, SnI_2 and SnF_2 were 250°C, 180°C and 170°C, respectively.

The tooling factors are primarily determined by the source–QCM–substrate geometry. Our vacuum chamber is equipped with four evaporation sources and four dedicated QCM sensors, arranged in a centro-symmetric configuration with respect to the substrate holder. As a result, the tooling factors are effectively equivalent for all sources and are dictated by the fixed chamber geometry rather than by the individual materials. Each precursor was calibrated independently at its specific source/QCM position. To target a desired stoichiometry, the deposition rates were not interpreted directly as molar ratios but were converted into molar fluxes by accounting for the molecular weight and bulk density of each material (assuming a deposition area of 1 cm^2, for simplicity). The evaporation rates were then adjusted accordingly. As an illustrative example, for the $Pb_{0.5}Sn_{0.5}I_2$ absorber with SnF_2 as a minor additive, PbI_2 and SnI_2 were deposited at identical thickness rates (0.5 Å s^{-1}) which, after correction for molecular weight and density, correspond to comparable molar deposition rates, while SnF_2 was introduced at a significantly lower molar flux. The corresponding parameters are summarized below:

PbI_2: (MM = 461 g mol^{-1}; d = 6.16 g cm^{-3}) for r = 0.5 Å s^{-1}, $r_{mol} \approx 0.07$ nmol s^{-1}
SnI_2: (MM = 373 g mol^{-1}; d = 4.97 g cm^{-3}) for r = 0.5 Å s^{-1}, $r_{mol} \approx 0.07$ nmol s^{-1}
SnF_2: (MM = 157 g mol^{-1}; d = 4.57 g cm^{-3}) for r = 0.03 Å s^{-1}, $r_{mol} \approx 0.01$ nmol s^{-1}

Perovskite Film Preparation. The inorganic seed layers were transferred to another N_2 glovebox for solution processing. A mixed cation solution of FAI, MAI and MACl (60 $mgml^{-1}$, 6 $mgml^{-1}$, and 6 $mgml^{-1}$, respectively) in iso-propanol or ethanol spin coated dynamically (40 s, 3500 rpm) on the evaporated $Pb_xSn_{(1-x)}I_2$ films. After spin coating, the substrates were annealed at 100°C for 1 min in the glovebox.

Device Fabrication. After perovskite conversion process, 20 nm of C60 and 7 nm of BCP were deposited in another evaporator with 0.5 Å s^{-1} (~390°C) and 0.2 Å s^{-1} (~130°C), respectively. Ag contacts (100nm) were evaporated within a metal evaporator using Ag pellets by applying currents ranging from 2.0-2.2 A. The fabricated devices were encapsulated with 30 nm of Al_2O_3 through atomic layer deposition in an Arradiance reactor at 40 °C in accordance with a published protocol.[1]

Measurements. Absorption spectroscopy measurements were performed with fiber optics based Avantes Avaspec2048 Spectrometer. For photoluminescence measurements, the films were illuminated with a diode laser of Integrated Optics, emitting at 515 nm and the spectra was obtained by Avantes Avaspec2048 spectrometer. The film thickness was measured by using a profilometer (Ambios, XP1). J–V characteristics were measured under AM 1.5G light (100 mW cm^{-2}) using a Wavelabs Sinus 70 LED solar simulator. Prior to measurements light intensity was calibrated using a calibrated Si reference diode. A Keithley 2612A source meter was used to record J-V curves, in a -0.2 and 0.8V voltage range, with 0.01 V steps and integrating the signal for 20 ms after a 10 ms delay, corresponding to a scan speed of ≈0.3 V s^{-1}. Masks with 0.05 cm^2 aperture area were placed on top of the cells during all measurements. The crystalline structure of films was studied by X-ray diffraction (XRD) and the data were collected in Bragg-Brentano geometry on an Empyrean PANalytical powder diffractometer with a copper anode operated at 45 kV and 40 mA. SEM images were taken using the Zeiss Gemini SEM 500 at 4 kV and 0.4 nA. Measurements of external quantum efficiency, internal quantum efficiency and reflection were made using the QE-R system by Enlitech®. For calibration of the EQE system, a silicon calibrated device is used (range from 300-1100nm), while for IQE, an integrating sphere is used, which allows to measure the

reflection of the sample, which is later used to calculate the internal quantum efficiency IQE by the formula $IQE = \frac{EQE}{1-R}$.

Diffusion length measurements. SSPG technique was measured using a configuration similar to the one reported.[2]The main idea of the technique is to measure a small change in sample conductivity (at a given voltage) in the presence of an optical grating, which is created by the division of a laser (633nm and 15mW of power in our case) by means of a beam splitter. The measurement is conducted under illumination of two beams I1 being the stronger one (95% or the total illumination) that sets the generation rate, and I2, that's is being chopped serving as a probe beam. The change in conductivity is directly measured on the sample using a lock-in amplifier for two configurations: when the two beams have orthogonal polarization states and therefore do not interfere (homogeneous illumination), followed by aligned polarization states, creating a periodic optical grating. The grating period Λ can be controlled by changing the angle between the two beams, which in our case is done by controlling a motorized linear stage which contains a mirror that redirects the weaker beam into 9 different mirrors, giving us a range of grating period Λ that goes from 0.9 μm up to 27 μm. The current generated is passed through a current/voltage amplifier and then sent to a Lock-In amplifier. The β parameter is then calculated as the ratio between the average of the measures with polarization and without it. Then the curve β vs Λ can be fitted using the formula:

$$\beta = 1 - \frac{2\vartheta}{\left(1 + \left(2\pi L_{diff}\right)^2\right)^2}$$

Which gives the diffusion length (Ldiff) and the constant ϑ associated with the interference quality.

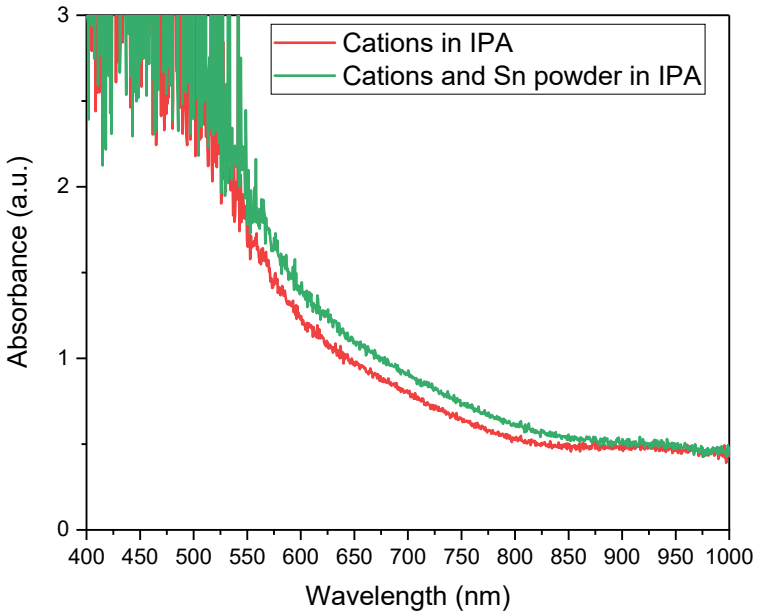

Figure S1 UV-vis spectra of the fabricated perovskite films.

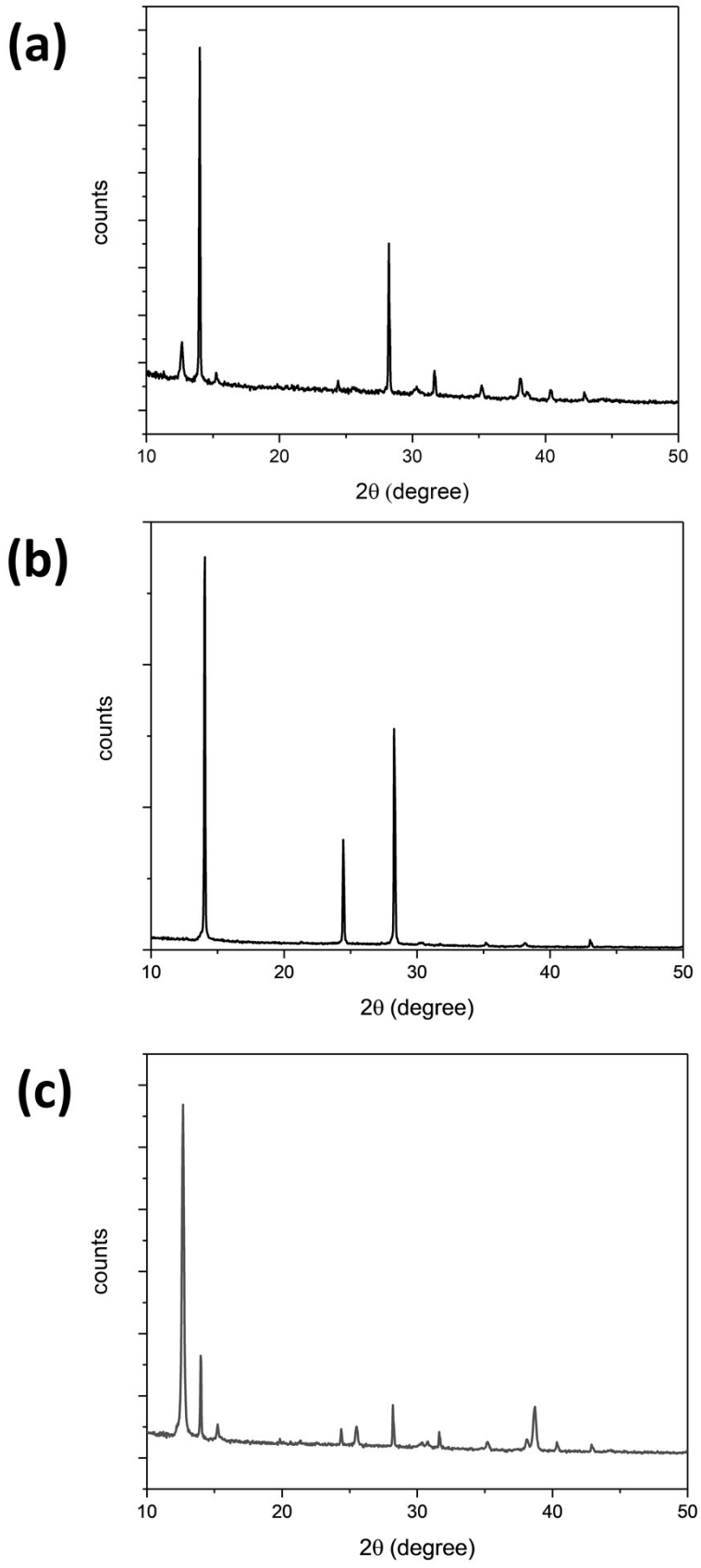

Figure S2 XRD data of $FA_{0.7}MA_{0.3}Pb_{0.5}Sn_{0.5}I_3$ perovskite on (a) ITO, (b) PEDOT:PSS, (c) PTAA substrates.

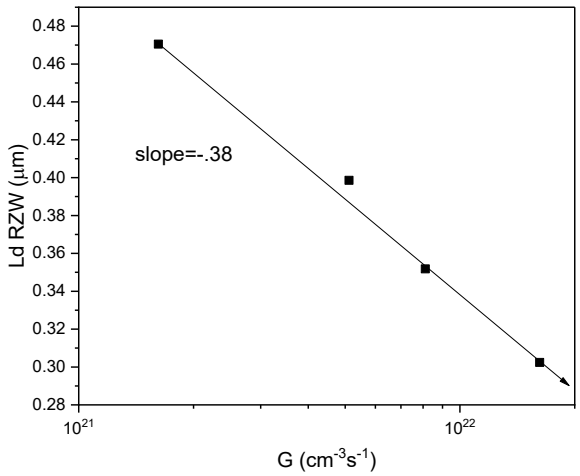

Figure S3 Change in diffusion lengths according to carrier generation.

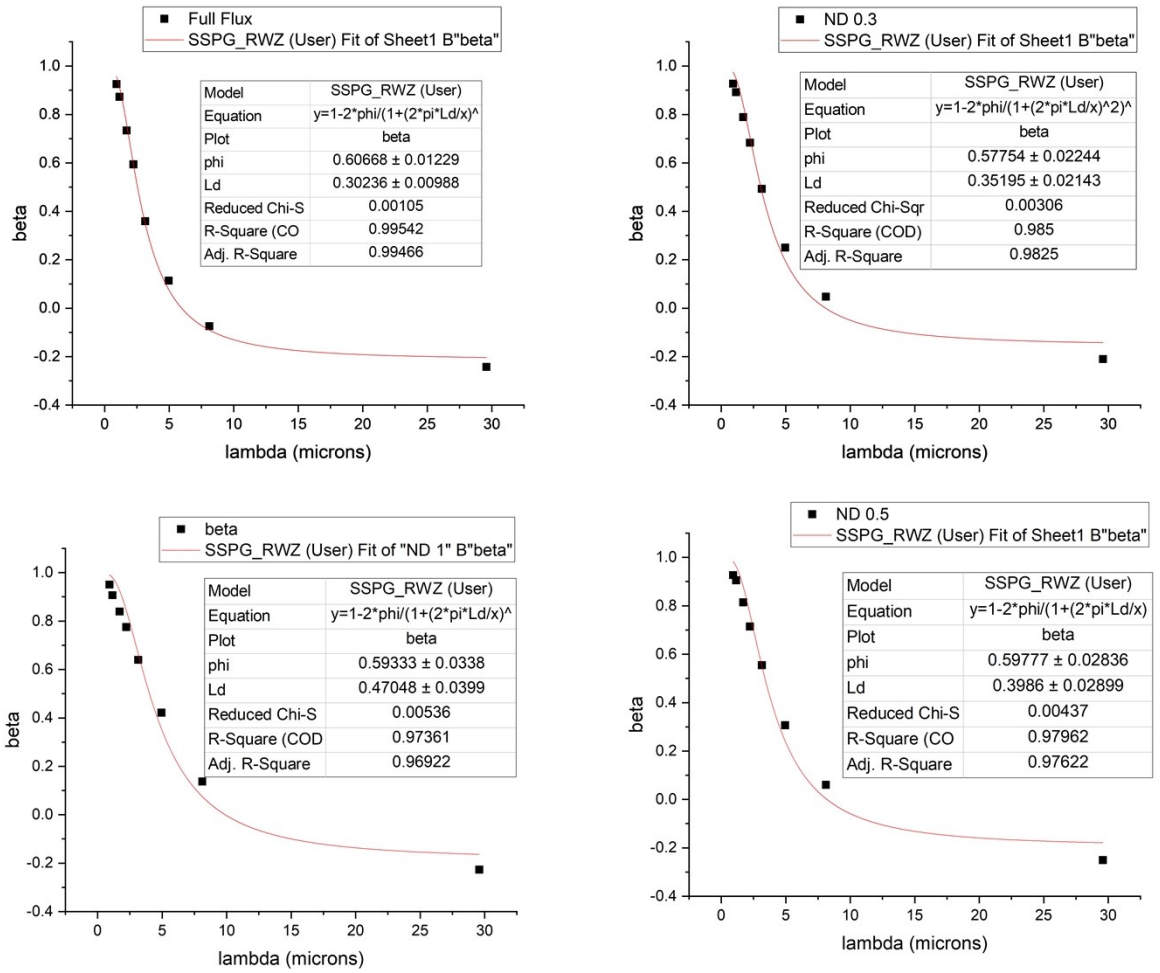

Figure S4 SSPG Analysis.

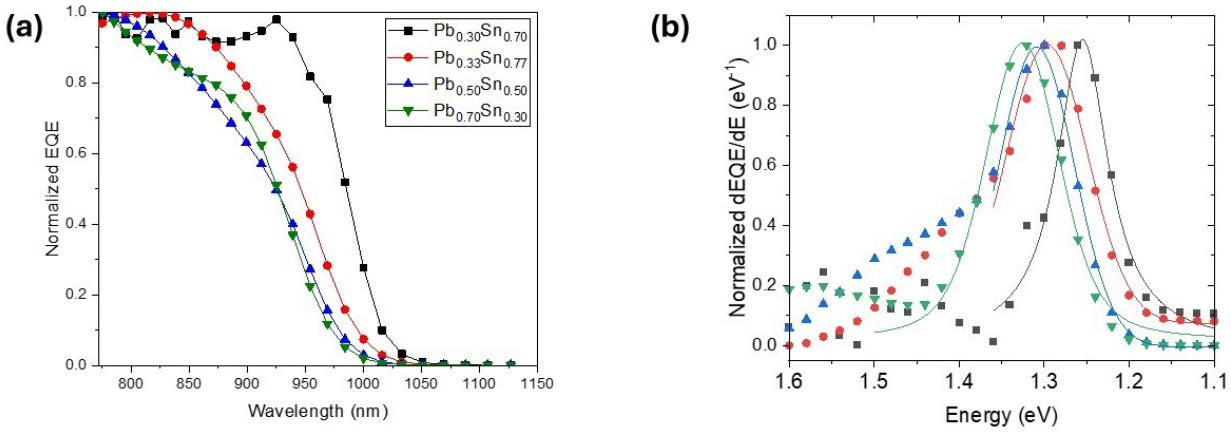

Figure S5 (a)Normalized EQE spectra at low energy region for different perovskites obtained by conversion of inorganic precursors with different compositions (b) Derivative of the normalized EQE spectrum

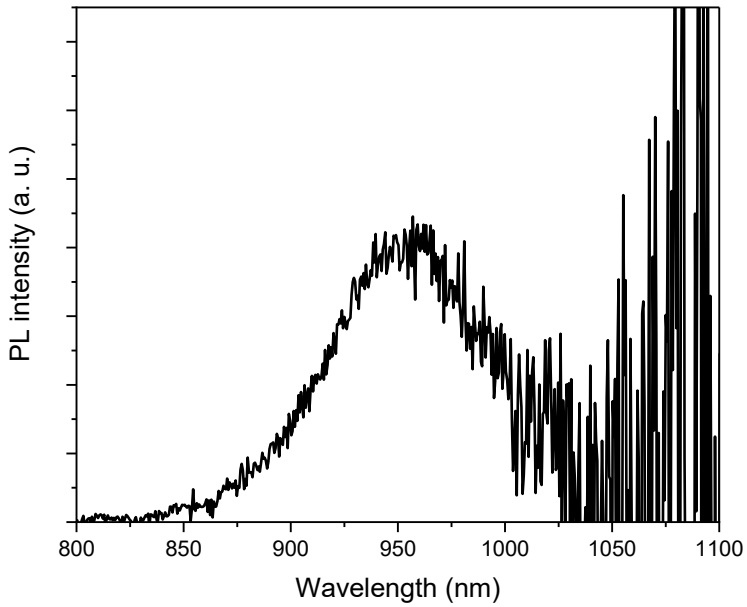

Figure S6 A typical PL image of a fabricated perovskite film.

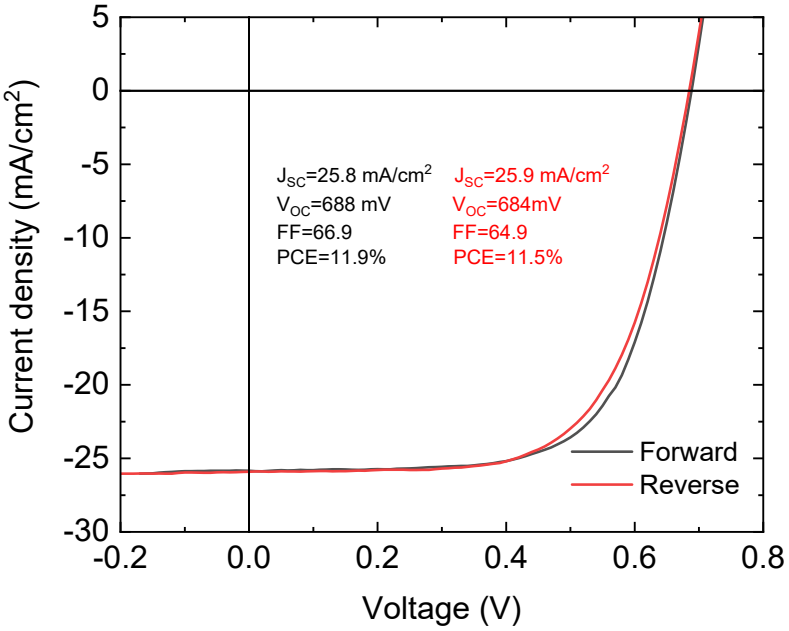

Figure S7 Photocurrent density vs voltage curves measured under standard AM 1.5G illumination for the champion device employing PEDOT:PSS as HTM.

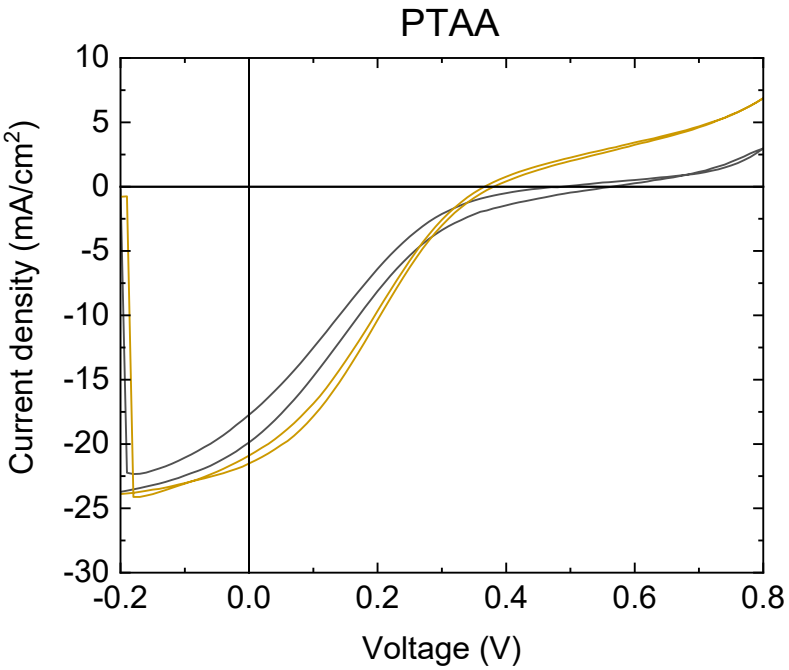

Figure S8 Photocurrent density vs voltage curves measured under standard AM 1.5G illumination for typical devices employing PTAA as HTM.

SCAPS-1D Simulations

In order to better elaborate on the changes in PV parameters with respect to the nominal Sn/Pb ratios, we simulated the J-V characteristics of the solar cells using $FA_{0.7}MA_{0.3}Pb_{0.3}Sn_{0.7}I_3$, $FA_{0.7}MA_{0.3}Pb_{0.5}Sn_{0.5}I_3$, and $FA_{0.7}MA_{0.3}Pb_{0.7}Sn_{0.3}I_3$ perovskites on ITO, using SCAPS-1D.[3] In the course of the simulations, bandgap values were those derived from EQE measurements, whereas other parameters were gathered from literature. Electron affinity (χ) and acceptor density (N_A) values were taken from the absolute energy-level measurements for tin and lead based perovskites[4] and from self-doping/redox trends,[5, 6] respectively. Interface-trap density (D_{it}) values were derived from perovskite/electron transport layer (ETL)[7]interface studies, and shunt resistance (R_{sh}) values were extracted by means of PSC modeling and standard J-V analysis methods[8, 9] to ensure that the simulated and experimental data aligns well (**Figure S9**). The set values for the parameters and the device metrics obtained through the simulations are given in **Table S1** (the information regarding the Global SCAPS settings, contact properties, layer profiles, and interface properties are provided in **TableS2-S4**). Our simulations reveal that higher J_{SC} values can be attributed to the lower acceptor density N_A and interface-trap density D_{it} values, with N_A having the stronger influence. In wider band gap compositions, the optical penalty is compensated by reduced recombination. Our simulations suggest that enhancement in V_{OC} values with increasing Pb content is predominantly resulting from the reduction of interface traps. Additionally, fill factor decreases mainly when the shunt resistances and acceptor densities are lower, indicating that higher leakage currents and weaker charge transport outweigh the positive effects of fewer interface traps. The device with 1.3 eV band gap shows slightly improved FF values, due to higher acceptor density and shunt resistance compared to the wider band gap device. The device with the lowest bandgap (1.26 eV) suffers from significant charge collection and recombination

losses resulting in markedly reduced J_{SC} and V_{OC} values but higher Rsh value allows better FF values.

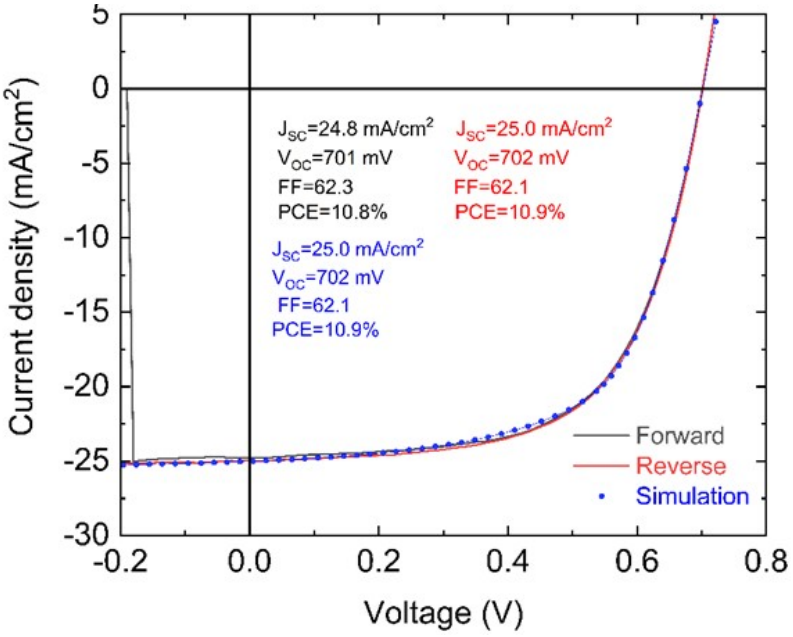

Figure S9 Measured and Simulated J-V Curves

Table S1: The parameters used for SCAPS-1D simulation and the resulting J-V metrics.

	$Pb_{0.3}Sn_{0.7}I_2$	$Pb_{0.5}Sn_{0.5}I_2$	$Pb_{0.7}Sn_{0.3}I_2$
Band gap E_g (eV)	1.26	1.30	1.32
Electron affinity (χ) (eV)	4.30	4.39	4.11
Acceptor doping (N_A) (cm^{-3})	4.68×10^{17}	4.79×10^{16}	1.20×10^{15}
Perovskite/ETL (D_{it}) (cm^{-2})	2.29×10^{12}	9.00×10^{11}	1.00×10^{9}
Shunt resistance (R_{sh}) ($\Omega.cm^2$)	7.44×10^{2}	2.91×10^{2}	2.00×10^{2}
Device metrics			
J_{SC} ($mA.cm^{-2}$)	14.0	22.7	25.1
V_{OC} (V)	0.65	0.70	0.72
FF (%)	67.2	59.4	55.2
PCE (%)	6.15	9.37	9.90

Table S2 Global SCAPS settings and contacts

Geometry, Scan, Illumination	
Illumination	From left (ITO/perovskite side), AM1.5G, 1 sun, 300K.[10]
Series / Shunt ($\Omega.cm^2$)	Rs=3.67; Rsh=Variable[8]
Contact optical filters	Transmission value = 0.82 (used as a flat front-side loss proxy).[11]
SCAPS contact mapping	
Left contact (front)	ITO/Glass; Flatband. [3] $S_n = 1 \times 10^2\ cm.s^{-1}$, $S_p = 1 \times 10^7\ cm.s^{-1}$ [3]
Right contact (Rear)	Ag; Work function $\Phi_m = 4.3\ eV$ [12] $S_n = 1 \times 10^7\ \ cm.s^{-1}$, $S_p = 1 \times 10^3\ cm.s^{-1}$ [3]

Table S3 Layer Profiles

Layer / parameter	$Perovskite$	$C_{60}\ (ETL)$	BCP
Thickness (nm)	430	20	7
Bandgap $E_g\ (eV)$	Variable	2.30 [13]	3.50 [14]
Electron affinity $\chi\ (eV)$	Variable	4.50 [15]	4.50 *
Dielectric permittivity ε_r (relative)	20 [16]	4 [[17]	3 [17]
Density of states $N_C = N_V$ (cm^{-3})	1×10^{18} [18]	1×10^{19} [19]	1×10^{19} [19]
Thermal velocities v_{th} ($cm.s^{-1}$)	$1 \times 10^7\ (n,p)$ [18]	$1 \times 10^7\ (n,p)$ [18]	$1 \times 10^7\ (n,p)$ [18]

Mobilities ($cm^2.V^{-1}.s^{-1}$)	$\mu_n = 2$ $\mu_p = 2$ [20]	$\mu_n = 1$ $\mu_p = 1 \times 10^{-3}$ [15]	$\mu_n = 1 \times 10^{-4}$ $\mu_p = 1 \times 10^{-8}$ [14]
Doping (cm^{-3})	$N_A = Variable$ $N_D = 1 \times 10^{14}$ [6]]	$N_A = 0$ $N_D = 1 \times 10^{16}$ [19]	$N_A = 0$ $N_D = 1 \times 10^{15}$ [19]
Radiative K_{rad} ($cm^3.s^{-1}$)	1×10^{-10} [21]	Default	Default
Bulk SRH density of recombination: N_t (cm^{-3})	8×10^{14} [22]	1×10^{14} [19]	1×10^{16} [19]
Bulk SRH cross sections: σ_n,σ_p (cm^2)	$\sigma_n = 1 \times 10^{-15}$ $\sigma_p = 1 \times 10^{-15}$ [23]	$\sigma_n = 1 \times 10^{-15}$ $\sigma_p = 1 \times 10^{-15}$ [23]	$\sigma_n = 1 \times 10^{-15}$ $\sigma_p = 1 \times 10^{-18}$ [23]
Bulk SRH defect energy level: E_t (eV)	0.60 above E_V [23]	0.30 above E_V [23]	0.50 above E_V [23]
Absorption model α_0 value (1/cm)	1.027×10^5 [24]	Default	Default
Sub-gap tail energy E_0 (eV)	0.0025 [25]	Default	Default

Note: "variable" in the perovskite column indicates composition-dependent values reported in main file **Table 1**.

*: BCP electron affinity (χ_{BCP}) was fixed to 4.50 eV as a numerical convenience to enforce an ohmic Ag/BCP/C_{60} contact and to avoid convergence errors [3]; this value is not claimed physically (physical value reported typically as ~ 3 eV [26]) and does not affect the composition-dependent trends, which are governed by the perovskite/C_{60} junction.

Table S4 Interface profile

	Perovskite/C_{60}	**C_{60}/BCP**
Energy reference E_t	single at 0.60 eV (above highest E_V) [23]	single at 0.60 eV (above highest E_V) [23]
Capture cross-	$\sigma_p = \sigma_n = 6 \times 10^{-16}$ [19, 23]	$\sigma_p = 1 \times 10^{-17}/\sigma_n = 1 \times 10^{-15}$

sections (cm^2)		[19, 23]
Defect density D_{it} (cm^{-2})	*Variable*	3×10^{10} [19]

References

[1] Kaya, I. C.; Zanoni, K. P. S.; Palazon, F.; Sessolo, M.; Akyildiz, H.; Sonmezoglu, S.; Bolink, H. J. Crystal Reorientation and Amorphization Induced by Stressing Efficient and Stable P–I–N Vacuum-Processed MAPbI3 Perovskite Solar Cells. *Advanced Energy and Sustainability Research*, **2021**, *2* (3), 2000065. https://doi.org/https://doi.org/10.1002/aesr.202000065.

[2] FathAllah, A.; Ventosinos, F.; Longeaud, C. An Automated Experiment for Determination of Thin Film Semiconductor Transport Parameters. *J. Phys. Conf. Ser.*, **2014**, *558* (1), 12011. https://doi.org/10.1088/1742-6596/558/1/012011.

[3] Burgelman, M.; Decock, K.; Niemegeers, A.; Verschraegen, J.; Degrave, S. SCAPS Manual. University of Gent (ELIS), "Most Recent Version."

[4] Tao, S.; Schmidt, I.; Brocks, G.; Jiang, J.; Tranca, I.; Meerholz, K.; Olthof, S. Absolute Energy Level Positions in Tin- and Lead-Based Halide Perovskites. *Nat. Commun.*, **2019**, *10* (1), 2560. https://doi.org/10.1038/s41467-019-10468-7.

[5] Meggiolaro, D.; Ricciarelli, D.; Alasmari, A. A.; Alasmary, F. A. S.; De Angelis, F. Tin versus Lead Redox Chemistry Modulates Charge Trapping and Self-Doping in Tin/Lead Iodide Perovskites. *J. Phys. Chem. Lett.*, **2020**, *11* (9), 3546–3556. https://doi.org/10.1021/acs.jpclett.0c00725.

[6] Savill, K. J.; Ulatowski, A. M.; Herz, L. M. Optoelectronic Properties of Tin–Lead Halide Perovskites. *ACS Energy Lett.*, **2021**, *6* (7), 2413–2426. https://doi.org/10.1021/acsenergylett.1c00776.

[7] Chouhan, A. S.; Jasti, N. P.; Avasthi, S. Effect of Interface Defect Density on Performance of Perovskite Solar Cell: Correlation of Simulation and Experiment. *Mater. Lett.*, **2018**, *221*, 150–153. https://doi.org/https://doi.org/10.1016/j.matlet.2018.03.095.

[8] Şahin, G.; Hakkı Alma, M. Study of the Static Characteristic I-V and the Electrical Parameters Corresponding to the Shunt Resistance Rsh and Series Resistance Rs per Unit Area of a Solar Cell with Grain Size. *Chinese Journal of Physics*, **2019**, *62*, 395–

404. https://doi.org/https://doi.org/10.1016/j.cjph.2019.09.034.

[9] Mortadi, A.; El Hafidi, E.; Nasrellah, H.; Monkade, M.; El Moznine, R. Analysis and Optimization of Lead-Free Perovskite Solar Cells: Investigating Performance and Electrical Characteristics. *Mater. Renew. Sustain. Energy*, **2024**, *13* (2), 219–232. https://doi.org/10.1007/s40243-024-00260-z.

[10] ASTM International. ASTM G173-03(2020): Standard Tables for Reference Solar Spectral Irradiances: Direct Normal and Hemispherical on 37° Tilted Surface; ASTM International: West Conshohocken, PA, 2020.

[11] Wisz, G.; Potera, P.; Sawicka-Chudy, P.; Gwóźdź, K. Optical Properties of ITO/Glass Substrates Modified by Silver Nanoparticles for PV Applications. *Coatings*, **2023**, *13* (1). https://doi.org/10.3390/coatings13010061.

[12] Michaelson, H. B. The Work Function of the Elements and Its Periodicity. *J. Appl. Phys.*, **1977**, *48* (11), 4729–4733. https://doi.org/10.1063/1.323539.

[13] Lof, R. W.; van Veenendaal, M. A.; Koopmans, B.; Jonkman, H. T.; Sawatzky, G. A. Band Gap, Excitons, and Coulomb Interaction in Solid ${\mathrm{C}}_{60}$. *Phys. Rev. Lett.*, **1992**, *68* (26), 3924–3927. https://doi.org/10.1103/PhysRevLett.68.3924.

[14] Gao, H.; Qin, C.; Zhang, H.; Wu, S.; Su, Z.-M.; Wang, Y. Theoretical Characterization of a Typical Hole/Exciton-Blocking Material Bathocuproine and Its Analogues. *J. Phys. Chem. A*, **2008**, *112* (38), 9097–9103. https://doi.org/10.1021/jp804308e.

[15] Pham, H. M.; Naqvi, S. D. H.; Tran, H.; Tran, H. Van; Delda, J.; Hong, S.; Jeong, I.; Gwak, J.; Ahn, S. Effects of the Electrical Properties of SnO2 and C60 on the Carrier Transport Characteristics of P-i-n-Structured Semitransparent Perovskite Solar Cells. *Nanomaterials*, **2023**, *13* (24). https://doi.org/10.3390/nano13243091.

[16] Samiee, M.; Konduri, S.; Ganapathy, B.; Kottokkaran, R.; Abbas, H. A.; Kitahara, A.; Joshi, P.; Zhang, L.; Noack, M.; Dalal, V. Defect Density and Dielectric Constant in Perovskite Solar Cells. *Appl. Phys. Lett.*, **2014**, *105* (15), 153502. https://doi.org/10.1063/1.4897329.

[17] Brebels, J.; Manca, J. V; Lutsen, L.; Vanderzande, D.; Maes, W. High Dielectric Constant Conjugated Materials for Organic Photovoltaics. *J. Mater. Chem. A Mater.*, **2017**, *5* (46), 24037–24050. https://doi.org/10.1039/C7TA06808E.

[18] Chen, Q.; Ni, Y.; Dou, X.; Yoshinori, Y. The Effect of Energy Level of Transport Layer on the Performance of Ambient Air Prepared Perovskite Solar Cell: A SCAPS-1D Simulation Study. *Crystals (Basel).*, **2022**, *12* (1). https://doi.org/10.3390/cryst12010068.

[19] AlZoubi, T.; Kadhem, W. J.; Al Gharram, M.; Makhadmeh, G.; Abdelfattah, M. A. O.; Abuelsamen, A.; AL-Diabat, A. M.; Abu Noqta, O.; Lazarevic, B.; Zyoud, S. H.; et al. Advanced Optoelectronic Modeling and Optimization of HTL-Free FASnI3/C60 Perovskite Solar Cell Architecture for Superior Performance. *Nanomaterials*, **2024**, *14* (12). https://doi.org/10.3390/nano14121062.

[20] Herz, L. M. Charge-Carrier Dynamics in Organic-Inorganic Metal Halide Perovskites. *Annu. Rev. Phys. Chem.*, **2016**, *67* (Volume 67, 2016), 65–89. https://doi.org/https://doi.org/10.1146/annurev-physchem-040215-112222.

[21] Johnston, M. B.; Herz, L. M. Hybrid Perovskites for Photovoltaics: Charge-Carrier Recombination, Diffusion, and Radiative Efficiencies. *Acc. Chem. Res.*, **2016**, *49* (1), 146–154. https://doi.org/10.1021/acs.accounts.5b00411.

[22] Siekmann, J.; Ravishankar, S.; Kirchartz, T. Apparent Defect Densities in Halide Perovskite Thin Films and Single Crystals. *ACS Energy Lett.*, **2021**, *6* (9), 3244–3251. https://doi.org/10.1021/acsenergylett.1c01449.

[23] Sabbah, H.; Arayro, J.; Mezher, R. Simulation and Investigation of 26% Efficient and Robust Inverted Planar Perovskite Solar Cells Based on GA0.2FA0.78SnI3-1%EDAI2 Films. *Nanomaterials*, **2022**, *12* (21). https://doi.org/10.3390/nano12213885.

[24] De Wolf, S.; Holovsky, J.; Moon, S.-J.; Löper, P.; Niesen, B.; Ledinsky, M.; Haug, F.-J.; Yum, J.-H.; Ballif, C. Organometallic Halide Perovskites: Sharp Optical Absorption Edge and Its Relation to Photovoltaic Performance. *J. Phys. Chem. Lett.*, **2014**, *5* (6), 1035–1039. https://doi.org/10.1021/jz500279b.

[25] Subedi, B.; Li, C.; Junda, M. M.; Song, Z.; Yan, Y.; Podraza, N. J. Effects of Intrinsic and Atmospherically Induced Defects in Narrow Bandgap (FASnI3)x(MAPbI3)1−x Perovskite Films and Solar Cells. *J. Chem. Phys.*, **2020**, *152* (6), 064705. https://doi.org/10.1063/1.5126867.

[26] Yoshida, H. Electron Transport in Bathocuproine Interlayer in Organic Semiconductor Devices. *The Journal of Physical Chemistry C*, **2015**, *119* (43), 24459–24464. https://doi.org/10.1021/acs.jpcc.5b07548.